Josephson Junctions and SQUIDs Created by Focused Helium-Ion-Beam Irradiation of $YBa_2Cu_3O_7$

B. Müller,[1,*] M. Karrer,[1] F. Limberger,[1] M. Becker,[1,2] B. Schröppel,[2] C.J. Burkhardt,[2] R. Kleiner,[1] E. Goldobin,[1] and D. Koelle[1]

[1] *Physikalisches Institut – Experimentalphysik II and Center for Quantum Science (CQ) in LISA$^+$, University of Tübingen, Auf der Morgenstelle 14, Tübingen 72076, Germany*

[2] *NMI Natural and Medical Sciences Institute at the University of Tübingen, Markwiesenstraße 55, Reutlingen 72770, Germany*

(Received 25 January 2019; published 25 April 2019)

By scanning with a 30-keV focused He ion beam (He-FIB) across $YBa_2Cu_3O_7$ (YBCO) thin-film microbridges, we create Josephson barriers with critical current density j_c adjustable by irradiation dose D. The dependence $j_c(D)$ yields an exponential decay. At 4.2 K, a transition from flux-flow to Josephson behavior occurs when j_c decreases below approximately 2 MA/cm^2. The Josephson junctions exhibit current-voltage characteristics (IVCs) that are well described by the resistively and capacitively shunted junction model, without excess current for characteristic voltages $V_c \lesssim 1$ mV. Devices on MgO and LSAT substrates show nonhysteretic IVCs, while devices on $SrTiO_3$ show a small hysteresis. For all junctions, an approximate scaling $V_c \propto j_c^{1/2}$ is found. He-FIB irradiation with a high dose produces barriers with $j_c = 0$ and high resistances of 10 kΩ to 1 GΩ. This provides the possibility to write highly resistive walls or areas into YBCO using a He-FIB. Transmission electron microscopy reveals an amorphous phase within the walls, whereas for lower doses the YBCO stays crystalline. We have also "drawn" superconducting quantum-interference devices (SQUIDs) by using a He-FIB for the definition of the SQUID hole and the junctions. The SQUIDs show high performance, with flux noise < 500 nΦ_0/Hz$^{1/2}$ in the thermal white-noise limit for a device with 19 pH inductance.

DOI: 10.1103/PhysRevApplied.11.044082

I. INTRODUCTION

Josephson junctions (JJs), i.e., weak links between two superconducting electrodes [1], are key elements in superconducting electronic circuits and are used both for basic studies of superconductivity and for many applications [2,3]. For conventional metallic superconductors, a mature trilayer thin-film technology based on Nb electrodes, separated by insulating or normal conducting barriers, has been well established for decades. This technology offers fabrication of JJs on a wafer scale with a small spread of characteristic parameters, such as critical current density j_0 and normal resistance times area ρ_n, even with lateral JJ size well below 1 μm [4,5].

For the high-transition temperature (high-T_c) cuprate superconductors, JJ technology is much less mature. Because of the complex nature of these materials, and in particular their small coherence length associated with strong sensitivity to defects on the atomic scale, a reliable trilayer JJ technology does not exist so far. On the other hand, the peculiar properties of cuprate superconductors, such as high T_c, large upper critical field, large energy gap, and d-wave symmetry of the superconducting order parameter, can provide major advantages, if JJ devices and circuits can be realized with sufficient control over JJ parameters. Promising examples are, e.g., in the field of terahertz generation [6], self-biased rapid single flux quantum circuits [7], or magnetometry based on superconducting quantum-interference devices (SQUIDs) [8,9].

Apart from intrinsic JJs in stacks of $Bi_2Sr_2CaCu_2O_{8+\delta}$ single crystals, used for terahertz generation [6], most developed cuprate JJs are based on epitaxially grown $YBa_2Cu_3O_{7-\delta}$ (YBCO) thin films with $T_c \approx 90$ K that also offer operation with cryocoolers or liquid nitrogen; a large variety of JJ types have been developed and their properties have been investigated [10–13].

Until recently, the most reliable, simple, and most frequently used high-T_c JJs have been YBCO grain-boundary (GB) JJs [11]. They are usually fabricated by the epitaxial growth of YBCO films on (rather expensive) bicrystal substrates from only a few materials. The GBJJs can be placed only along the single GB line, which not only imposes topological limitations, but also limits the complexity of feasible circuits. The more advanced biepitaxial

*benedikt.mueller@uni-tuebingen.de

 © 2019 American Physical Society

technique allows one to fabricate so-called tilt-twist GBs [12]. Such GBJJs can be distributed all over the chip and one can even fabricate 0-π JJs [14]. Still, GBJJs suffer from hardly controllable inhomogeneity along the GB line, which makes the properties of the JJs not very reproducible and causes a substantial spread in JJ parameters. Alternative approaches to create Josephson barriers in cuprates are based on local irradiation of thin films with a high-energy focused electron beam [15–18] or on irradiation with high-energy ions (protons [18], neon [19,20], oxygen [21,22]) through a lithographically defined mask with a nanogap. The local irradiation drives the material from the superconducting to the normal conducting or even insulating state. So far, this approach has been hampered by the fact that it was not possible to create ultrathin Josephson barriers that would provide JJs with high characteristic voltage $V_c = j_0\rho_n$ and current-voltage characteristics (IVCs) without excess current that are well described by the resistively and capacitively shunted junction (RCSJ) model [23,24]. This is an important prerequisite for many applications. For reviews on various approaches to modify the properties of cuprate superconductors by local irradiation, see, e.g., Refs. [25,26] and references therein.

With the recent development of helium ion microscopy (HIM) [27], a sharply focused He ion beam with an approximately 0.5-nm diameter can be used to irradiate and modify cuprate superconductors on the nanoscale. This approach has been successfully used by Cybart and co-workers to fabricate JJs using focused helium-ion-beam (He-FIB) irradiation of YBCO thin films, and they demonstrated that the barriers in such He-FIB JJs can be changed continuously from conducting to insulating by varying the irradiation dose [28]. Moreover, the same group demonstrated already the integration of He-FIB JJs into SQUID devices [29], and the feasibility to use high-dose irradiation for nanoscale patterning (without removing material) in YBCO devices [30,31]. For a short review on this approach, also including irradiation with a focused Ne ion beam, see Ref. [32]. First attempts to extend this technique to the fabrication of JJs in other cuprate materials have been reported [33], and the creation of JJs in MgB_2 thin films by He-FIB irradiation has been demonstrated very recently [34].

Here, we report on the realization of He-FIB JJs in YBCO thin films on different substrates. We focus on the analysis of the electric-transport properties at 4.2 K of such JJs, complemented by numerical simulations based on the RCSJ model and on the dependence of the JJ properties on irradiation dose. We also present results on scanning transmission electron microscopy analysis of the local structural modification of the YBCO films, which can be made highly resistive by He-FIB irradiation with a high dose. The latter feature has been used to fabricate SQUIDs, by combination of medium-dose irradiation to produce two JJs with high-dose irradiation to produce the SQUID loop, and we demonstrate dc SQUID operation, including low-noise performance.

II. DEVICE FABRICATION

We fabricate epitaxially grown *c*-axis-oriented YBCO thin films of thickness d by pulsed laser deposition (PLD) on various single-crystal (001)-oriented $SrTiO_3$ (STO), MgO, and $(LaAlO_3)_{0.3}(Sr_2AlTaO_6)_{0.7}$ (LSAT) substrates (10×10 mm^2). The crystalline quality of the YBCO films is characterized by x-ray diffraction to determine the full width at half maximum (FWHM) of the rocking curve of the YBCO (005) peak and to extract d via Laue oscillations at the YBCO (001) Bragg peak. YBCO films on STO substrates are covered *in situ* by an epitaxially grown STO cap layer with a thickness of 10 unit cells (3.9 nm). For details on the PLD growth of our YBCO films on STO substrates, as well as their structural and electric-transport properties, see Refs. [35,36].

For electrical contacts on STO and MgO chips, we photolithographically define a resist mask, covering the central area of the chips, remove an approximately 10-nm-thick surface layer (including the STO cap layer) by Ar ion milling, and *in situ* deposit a Au film by magnetron sputtering, followed by a lift-off process. For electrical contacts on LSAT chips, we deposit in-situ, after the PLD process, a Au film onto the YBCO by in-situ electron beam evaporation after the PLD process. Subsequently, we photolithographically define a resist mask, covering the outer area of the chips, and remove the Au film on the central area of the chip by Ar ion milling.

Afterward, we use photolithography and Ar ion milling to prepattern 156 YBCO microbridges of width $w \approx 4$ μm (and length ≈ 200 μm) on each chip for He ion irradiation and electric-transport measurements in a four-point configuration. Table I gives an overview of the five chips, with some basic properties of their YBCO microbridges, which have been used for fabricating devices via He-FIB irradiation. A specific bridge on one of the chips is labeled by the chip name, followed by -*n* for bridge number *n*, e.g., STO-1-4 corresponds to bridge number 4 on the chip STO-1.

TABLE I. Properties of studied chips with YBCO thin film microbridges used for fabricating He-FIB-irradiated devices. To calculate the effective penetration depth $\lambda_{\text{eff}} = \lambda_L^2/d$, we assume a London penetration depth $\lambda_L = 250$ nm.

Chip (substrate)	T_c (K)	FWHM (deg)	d (nm)	w (μm)	λ_{eff} (μm)
STO-1	89	0.11	50	3.2	1.25
STO-2	89	0.15	29	4.0	2.16
STO-3	91	0.08	46	3.8	1.36
MgO-1	89	0.17	53	4.1	1.18
LSAT-1	86	0.07	50	4.4	1.25

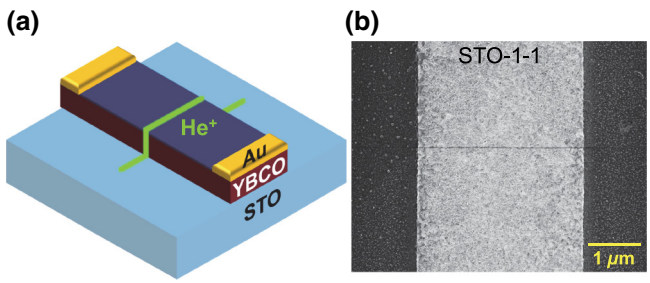

FIG. 1. (a) Schematic illustration of the He-FIB JJ geometry. (b) SEM image of a JJ (visible as thin dark line) fabricated with $D = 600$ ions/nm.

After prepatterning the YBCO microbridges, focused He-ion-beam irradiation is done in a Zeiss Orion NanoFab He/Ne ion microscope (HIM) with 30-keV He^+ ions. A beam current of 200 fA is used, and the beam is focused to a nominal diameter of 0.5 nm. A dwell time of 1 μs is used to irradiate line patterns with a dwell point spacing of 0.25 nm, which corresponds to a single linescan dose $D_{SL} = 5$ ions/nm. To obtain a certain line dose $D = Nd_{SL}$, a single linescan is repeated N times. To irradiate an area, adjacent linescans are offset by $\Delta = 0.25$ nm. In that case, a line dose of, e.g., $D = 100$ ions/nm corresponds to an area dose of $D_A \equiv D/\Delta = 400$ ions/nm^2 or 4×10^{16} ions/cm^2.

Figure 1(a) schematically illustrates the sample geometry and irradiation process for a single JJ. A scanning electron microscopy (SEM) image of STO-1-1 fabricated with $D = 600$ ions/nm is shown in Fig. 1(b). The irradiated linescan appears as a dark line in the SEM image due to He-FIB-induced carbon deposition from residual gas inside the He ion microscope chamber.

III. YBCO BRIDGES WITH HE-FIB-INDUCED BARRIERS AND JOSEPHSON JUNCTIONS

In this section, we present results obtained from devices fabricated on the chips listed in Table I.

A. Resistance vs temperature

Figure 2 shows measurements of the resistance R (at constant bias current $I_b = 1$ μA) vs temperature T of two YBCO microbridges. The $R(T)$ curve of STO-1-2, measured before He ion irradiation, shows a decrease of the resistance by about a factor of 3 from 300 to 100 K, with resistivity $\rho(100\,\text{K}) \approx 190\,\mu\,\Omega$cm, followed by a sharp transition to $R < 1\,\Omega$ at $T_c = 89$ K. After irradiation with $D = 700$ ions/nm (and thus producing a JJ), the $R(T)$ curve of STO-1-2 shows an additional footlike structure with a plateau at $R = 6.6\,\Omega$ between approximately 40 K and T_c (see inset). This foot structure is due to thermally activated phase slippage [37] causing a finite voltage

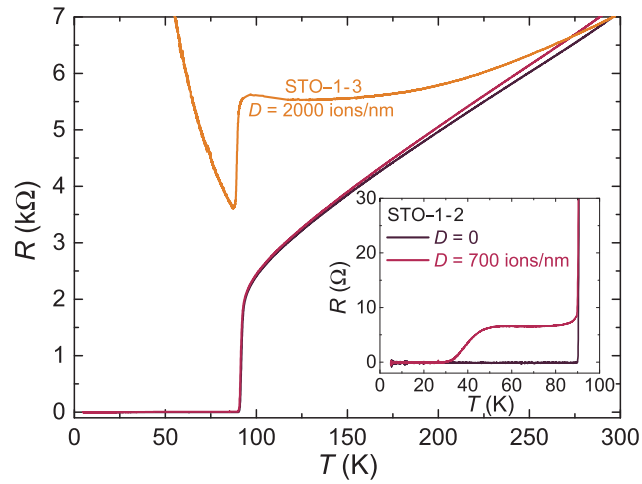

FIG. 2. $R(T)$ dependence of YBCO bridge STO-1-2 before and after irradiation and of STO-1-3 after irradiation. The inset shows an enlargement of the resistive transitions of STO-1-2.

drop across the JJ when (upon increasing T) the thermal energy $k_B T$ approaches the Josephson coupling energy $E_J = I_0 \Phi_0/(2\pi)$. Here, I_0 is the noise-free critical current of the JJ (which decreases with increasing T) and Φ_0 is the magnetic flux quantum. Accordingly, the plateau reflects the situation when the measurable critical current I_c drops below the bias current I_b, causing the JJ to reach its normal state resistance R_n. He-FIB irradiation with a high dose fully suppresses I_c. This is shown in Fig. 2 for sample STO-1-3, which has been irradiated with $D = 2000$ ions/nm. At $T = 4.2$ K, the resistance is $> 20\,\text{k}\Omega$.

B. Transmission electron microscopy analysis

By the combination of atomic force microscopy and scanning near-field optical microscopy, it has been shown by Gozar *et al.* [33] that He-FIB irradiation with doses above 10^{18} ions/cm^2 induces amorphous tracks in $La_{1.84}Sr_{0.16}CuO_4$ thin films with a substantial lateral width of approximately 500 nm. In contrast to this, He-FIB produced JJs in YBCO films have been reported to show IVCs well described by the RCSJ model, indicating much less lateral damage [28]. However, no results have been reported on microstructural changes induced by a He-FIB in YBCO films so far.

To image possible structural modifications induced by He-FIB irradiation in our YBCO films, we use scanning transmission electron microscopy (STEM). For the STEM studies, we irradiate the YBCO bridge STO-1-4 with a series of 14 parallel lines using increasing doses from $D = 50$ to 10^5 ions/nm, with well-defined spacing (200 nm in most cases) between adjacent lines. Subsequently, we prepare a cross-sectional TEM lamella containing all irradiated lines, by *in situ* lift-out using a Ga-FIB microscope together with a micromanipulator. Figures 3(a)–3(d)

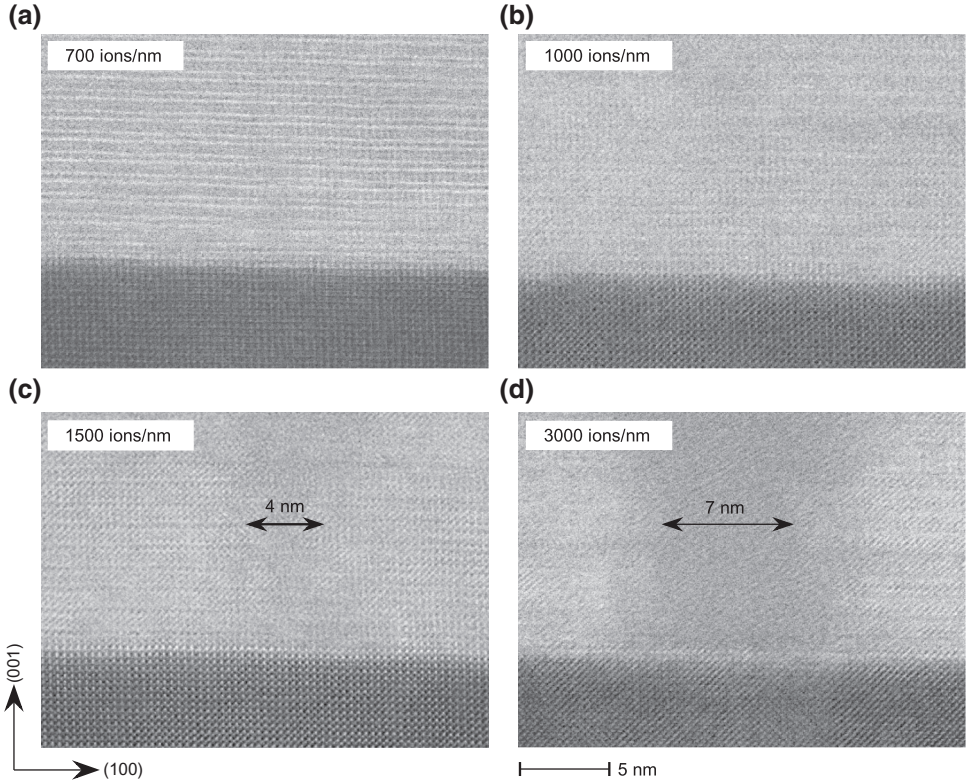

FIG. 3. Cross-section STEM images of the YBCO/STO interface (top/bottom, respectively) at the location of He-FIB irradiation with increasing dose D from (a) to (d). Arrows indicate the widths of amorphous regions.

show cross-section STEM images, viewed along the [010] zone axis, of four regions of the bottom part of the YBCO film at the YBCO/STO interface that are irradiated with $D = 700$, 1000, 1500, and 3000 ions/nm, respectively. The areas that are irradiated with $D \geq 3000$ ions/nm can be easily located in the STEM images due to significant changes in the microstructure of the YBCO films. As we know the exact spacing between the different areas irradiated along the lamella, we can also easily localize in the STEM images the areas that have been irradiated with lower D. For $D = 700$ and 1000 ions/nm [cf. Figs. 3(a) and 3(b)], we cannot identify any change in the structure of the irradiated sections. For $D = 1500$ ions/nm, an amorphous track of width $w_a \approx 4$ nm appears [cf. Fig. 3(c)], increasing to $w_a \approx 7$ nm for $D = 3000$ ions/nm [cf. Fig. 3(d)]. We note that with further increasing D, the amorphous track width w_a increases roughly linearly up to approximately 170 nm for the highest dose $D = 10^5$ ions/nm that we investigate.

Our STEM analysis indicates that medium doses do not induce significant structural damage of the YBCO crystal lattice, which is consistent with the assumption that the He-FIB easily moves oxygen ions from the Cu-O chains to interstitial sites [30], thereby altering the local electric-transport properties of YBCO on the nanometer scale without destroying the crystal lattice as a whole. Hence, He-FIB irradiation with a medium dose seems to be a very promising approach for creating JJs in YBCO. Moreover, we find that irradiation with larger doses of some 1000 ions/nm induces amorphous, and hence presumably highly resistive, regions, but still with a relatively small lateral extension of only a few nanometers.

C. Transport characteristics of He-FIB-induced Josephson junctions

In the following, we present electric-transport characteristics of approximately 50 YBCO brides that are irradiated with doses up to $D = 800$ ions/nm to produce JJs. We measure IVCs, i.e., current I vs voltage V, and the modulation of the critical current I_c in an externally applied magnetic field B (perpendicular to the substrate plane) in an electrically and magnetically shielded environment, with the samples at $T = 4.2$ K immersed in liquid He.

For all devices exhibiting IVCs that can be described by the RCSJ model, we perform numerical simulations, including thermal noise, to determine their noise-free critical current I_0, normal resistance R_n, and capacitance C. From these simulations, we determine the Stewart-McCumber parameter $\beta_C \equiv 2\pi I_0 R_n^2 C/\Phi_0$ and also the amount of excess current I_e, if present.

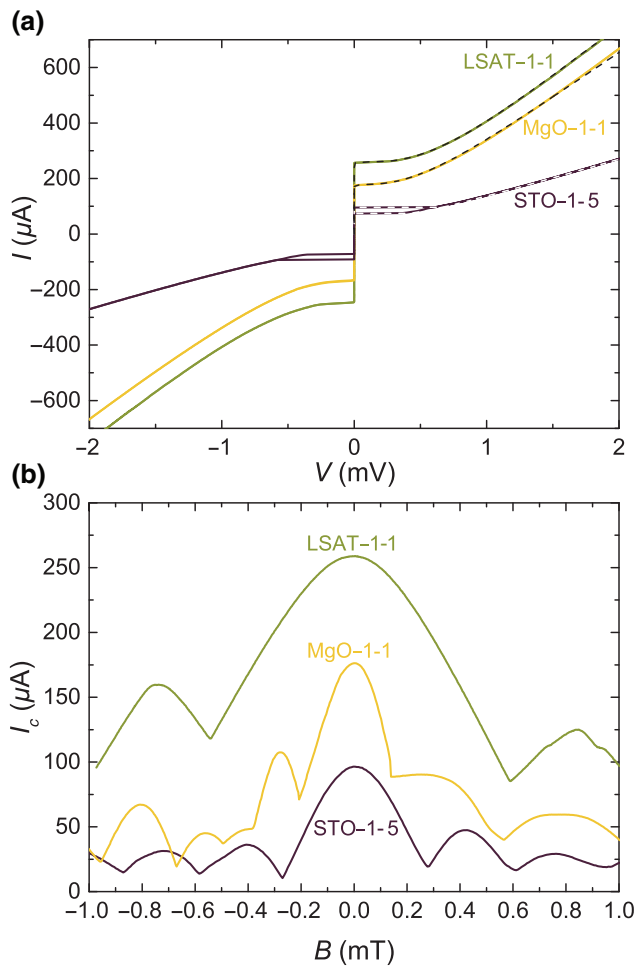

FIG. 4. Electric-transport characteristics of He-FIB JJs fabricated on different substrates: (a) IVCs showing experimental data (solid lines) and numerical simulation results for $I > 0$ (dashed lines) and (b) $I_c(B)$ patterns.

Figure 4 shows a representative set of IVCs [Fig. 4(a)] and $I_c(B)$ patterns [Fig. 4(b)] for JJs on different substrate materials. Irradiation doses and characteristic JJ parameters are given in Table II. As shown by the simulated curves [dashed lines in Fig. 4(a)], the IVCs can be well described by the RCSJ model and do not show any excess current. Only the JJ on STO shows a hysteresis in the IVC, with a JJ capacitance $C = 0.17\,\text{pF}$ and $\beta_C = 2.77$ obtained from simulations. Data regarding β_C for all JJs are presented and discussed at the end of this section.

The $I_c(B)$ patterns shown in Fig. 4(b) exhibit clear modulation of the critical current with applied magnetic field; however, they significantly deviate from the Fraunhofer-like shape expected for homogeneous JJs in the short junction limit $w \lesssim 4\lambda_J$, where

$$\lambda_J = \sqrt{\frac{\Phi_0}{2\pi\mu_0 d_{\text{eff}} j_0}} \tag{1}$$

is the Josephson penetration depth with the effective JJ inductance $\mu_0 d_{\text{eff}}$. Our YBCO films grown on STO have a London penetration depth $\lambda_L \approx 250$ nm [38–41]. Therefore, the devices discussed here are clearly in the thin-film limit $d \ll \lambda_L$ and, hence, the effective penetration depth $\lambda_{\text{eff}} = \lambda_L^2/d$ (see Table I) should be used to determine $d_{\text{eff}} = 2\lambda_{\text{eff}}$ in Eq. (1). Thus, we obtain the values of λ_J listed in Table II and see that all JJs are in the long JJ limit ($w > 4\lambda_J$).

Moreover, since $\lambda_J \ll \lambda_{\text{eff}}$, these JJs are in the nonlocal regime [42–46]. In this regime, the $I_c(B)$ patterns can be calculated analytically [42,46] only in the narrow JJ limit, i.e., for $w < \lambda_{\text{eff}}$ and $w < \lambda_J^{\text{NL}}$, where $\lambda_J^{\text{NL}} = \lambda_J^2/d$ is a nonlocal Josephson length [42]; see Table II. In our case, the above conditions are not really satisfied. Thus, our JJs are in the intermediate regime, where the exact shape of $I_c(B)$ is not known. However, we can roughly estimate the value of the penetration field B_{c1} [defined as a continuation of the first lobe of the $I_c(B)$ dependence down to $I_c = 0$] using (i) the local long JJ model and (ii) the narrow nonlocal JJ model [42] and compare them with experimentally measured values of B_{c1}^{ex}, given in Table II. The local long JJ model yields $B_{c1}^{\text{LO}} = \Phi_0/(\pi d_{\text{eff}}\lambda_J)$, whereas for a nonlocal narrow JJ [42], $B_{c1}^{\text{NL}} = \Phi_0/(0.715w^2)$ (independent of j_0). By comparing these values with the experimental ones (see Table II), we see that B_{c1}^{ex} for STO-1-5 and MgO-1-1 are better described by the nonlocal theory, while B_{c1}^{ex} for LSAT-1-1 is closer to a local long JJ.

A detailed study of the $I_c(B)$ patterns of our He-FIB-induced JJs is out of the scope of the work presented here. Typically, our JJs on MgO have more irregular $I_c(B)$ patterns than those on STO and LSAT [cf. Fig. 4(b)]. This result indicates more inhomogeneous barrier properties of He-FIB-induced JJs on MgO and may either be attributed to the much larger lattice mismatch between MgO and YBCO and correspondingly poorer crystalline quality of

TABLE II. Irradiation doses and device parameters of JJs shown in Fig. 4.

	D (ions/nm)	I_0 (μA)	R_n (Ω)	V_c (μV)	C (pF)	β_C	λ_J (μm)	λ_J^{NL} (μm)	B_{c1}^{ex} (mT)	B_{c1}^{LO} (mT)	B_{c1}^{NL} (mT)
STO-1-5	700	99	7.44	737	0.17	2.77	0.42	1.8	0.31	0.63	0.28
MgO-1-1	500	178	3.07	546	0.15	0.77	0.37	2.6	0.25	0.75	0.17
LSAT-1-1	200	260	2.69	699	0.15	0.83	0.30	3.5	0.76	0.88	0.15

YBCO films or stronger charging of the MgO substrates that is observed during the He-FIB process.

In the following, we analyze the scaling of characteristic JJ properties j_c, ρ_n, and $j_c\rho_n$ with irradiation dose D. Note that devices irradiated with the lowest doses do not show JJ behavior. Therefore, we denote here all critical current densities as j_c. For all devices showing RCSJ behavior, however, the values given here refer to the noise-free values of j_0 obtained from numerical simulations.

Figure 5(a) summarizes $j_c(D)$ for all investigated devices. We attribute the significant scatter (cf. e.g., the data points for 700 ions/nm on STO-1) to instabilities in the fabrication process that we have not yet optimized. For instance, slight variations in the He-FIB focus spot size and beam current both affect the barrier properties. In spite of this scatter, we clearly find an exponential decay $j_c(D) \approx j_{c,0}\exp(-D/D_0)$, with $j_{c,0} = 3 \times 10^7\,\mathrm{A/cm^2}$ and with $D_0 = 38$ ions/nm for LSAT-1 and $D_0 = 130$ ions/nm for the other chips. The reason for the much stronger decay of $j_c(D)$ on LSAT compared to the devices on STO or MgO has not been clarified yet. Clearly, we do not find a correlation of D_0 with YBCO film thickness or crystalline quality (cf. FWHM values in Table I).

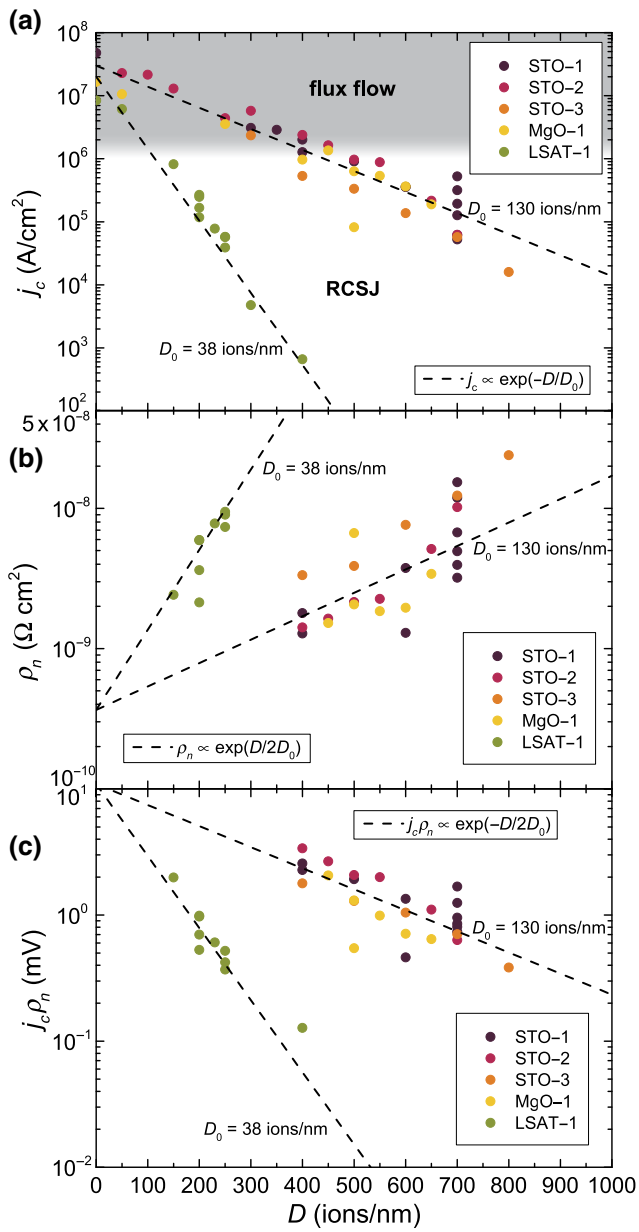

FIG. 5. Dependence of device parameters on He ion line dose D for various samples on different substrates: (a) $j_c(D)$, (b) $\rho_n(D)$, and (c) $j_c\rho_n(D)$. The dashed lines indicate the approximate scaling behavior as discussed in the text.

For $j_c \lesssim 2\,\mathrm{MA/cm^2}$, the IVCs show RCSJ-like behavior, whereas devices with higher critical current densities yield flux-flow-type IVCs, as indicated by the gray area in Fig. 5(a). Altogether, the range of variation of j_c covers 5 orders of magnitude. We note that an exponentially decaying behavior of j_c is well known from cuprate grain boundaries, where j_c decays exponentially with the grain-boundary misorientation angle Θ [11,47,48]. In a theoretical analysis of cuprate grain-boundary JJs, Graser *et al.* [48] related the exponential decay of $j_c(\Theta)$ to charging of the interface near defects induced by the structural distortions at the grain boundary. For the He-FIB-induced JJ barriers, the locally induced defect structure is not known yet, and it remains to be clarified whether a similar charging mechanism is responsible for the exponential decay of $j_c(D)$. A simple explanation of the exponential decay of j_c with increasing D would be a linear increase of the JJ barrier thickness. As stated in Sec. B, the STEM analysis yields a roughly linear increase of the amorphous track width with increasing D for doses above 1000 ions/nm. However, for lower doses, the STEM data do not allow us to make a statement on the width of the induced defect regions and their scaling with D.

Our analysis of the IVCs of He-FIB JJs produced with variable doses also yields a systematic scaling of the resistance times area product $\rho_n \equiv R_n wd \approx \rho_{n,0}\exp(D/2D_0)$ with $\rho_{n,0} = 0.37\,\mathrm{n\Omega\,cm^2}$; i.e., ρ_n increases exponentially with D as shown in Fig. 5(b). Interestingly, the stronger decay of $j_c(D)$ for JJs on LSAT comes along with a correspondingly stronger increase in $\rho_n(D)$; i.e., we can use the same values of D_0 for the scaling of $\rho_n(D)$ as used for the scaling of $j_c(D)$. Accordingly, the characteristic voltage $V_c = j_c\rho_n$ also shows an exponential scaling $V_c \approx V_{c,0}\exp(-D/2D_0)$ with $V_{c,0} = j_{c,0}\,\rho_{n,0} = 11\,\mathrm{mV}$, as shown in Fig. 5(c). We note here that Figs. 5(b) and 5(c) contain only data points that correspond to RCSJ-type IVCs.

The fact that our analysis of the scaling of characteristic JJ properties (j_c, ρ_n, and V_c) with D can be described by the same values of D_0 indicates a universal scaling of V_c with either j_c or ρ_n independent of substrate material. This result is shown in Fig. 6, where we display $V_c(j_c)$ and $V_c(\rho_n)$ for all investigated JJs. Despite the

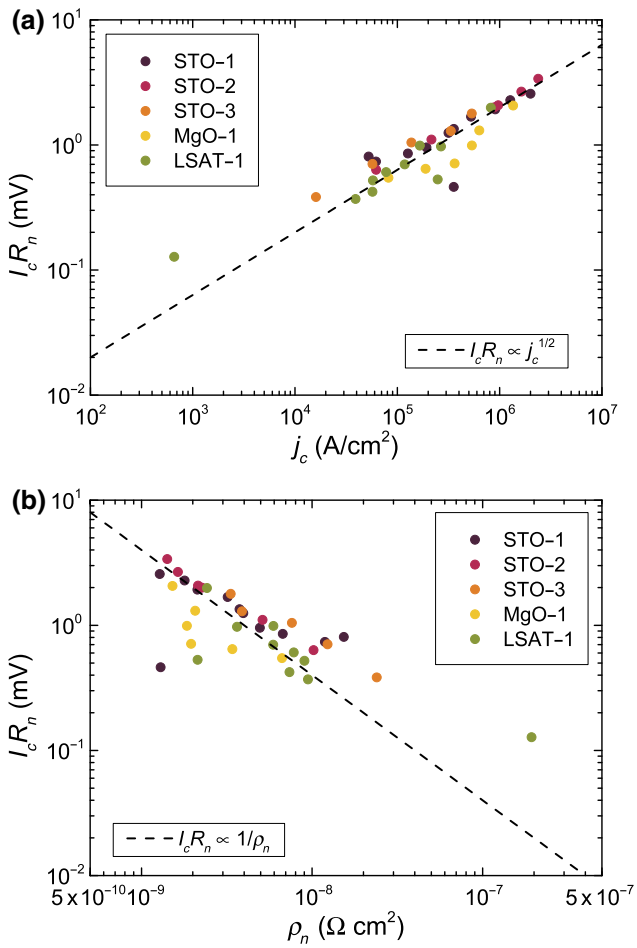

FIG. 6. Characteristic voltage I_cR_n for He-FIB JJs with RCSJ-like IVCs on different substrates (a) vs critical current density j_c and (b) vs resistance times area ρ_n. Dashed lines indicate $I_cR_n \propto \sqrt{j_c}$ in (a) and $I_cR_n \propto 1/\rho_n$ in (b) as discussed in the text.

significant scatter in the data, a clear trend is visible, which can be described by $I_cR_n \approx V_{c,1}(j_c/j_{c,1})^{1/2}$ [dashed line in Fig. 6(a)], with $V_{c,1} = 2\,\mathrm{mV}$ and $j_{c,1} = 10^6\,\mathrm{A/cm^2}$ and by $I_cR_n \approx V_{c,1}(\rho_{n,1}/\rho_n)$ [dashed line in Fig. 6(b)] with $\rho_{n,1} = 2\,\mathrm{n\Omega\,cm^2}$. We note that an approximate scaling $I_cR_n \propto \sqrt{j_c}$ and $I_cR_n \propto 1/\rho_n$ has also been observed for many cuprate grain-boundary JJs and other JJ types in cuprate superconductors, albeit with a slightly larger $V_{c,1}$ for the same $j_{c,1}$ and $\rho_{c,1}$ [10]. However, we should also note that the existence or absence of a universal scaling of I_cR_n vs j_c or ρ_n for all cuprate JJs and the origin of such a scaling has been discussed controversially in the literature; see, e.g., Refs. [10,11,16]. At least, for oxygen-depleted grain boundaries [11], there seems to be consensus on the same scaling as we see in our He-FIB JJs. This result is probably not surprising, because the He-FIB irradiation induces such an oxygen depletion [28].

So, obviously, for achieving large values of V_c, one should use doses that are as small as possible to obtain large values of j_c, but still provide JJs with RCSJ-type IVCs. Moreover, for fabricating SQUIDs (cf. Sec. IV), one wants to have nonhysteretic IVCs, i.e., $\beta_C \lesssim 1$. To address these issues, we determine from RCSJ simulations the dependencies of β_C and of the excess current densities j_e of our He-FIB JJs on j_c.

Figure 7(a) shows $\beta_C(j_c)$. We clearly find a significant difference for devices on STO as compared to those on LSAT or MgO. While for devices on LSAT and MgO the values of β_C are essentially independent of j_c and yield values between approximately 0.5 and 1, for devices on STO, β_C is always above 1 (up to approximately 4) and decays with increasing j_c. This result reflects the fact that we observe hysteretic IVCs at 4.2 K for all JJs on STO substrates and nonhysteretic IVCs for all JJs on MgO and LSAT. We attribute this behavior to a significant stray capacitance contribution caused by the large permittivity of STO at low T [49]. However, a more detailed analysis of this behavior would require a systematic variation of the JJ width, which we do not perform for the present study. For YBCO grain-boundary JJs, the capacitance C per area A has been found to vary roughly [11] within 10^{-6} to 10^{-4} F/cm^2, with a significant increase with increasing j_c from roughly 10^3 to 10^6 A/cm^2. In contrast, for our He-FIB JJs, we find for most devices C/A to scatter within the range from 5×10^{-5} to 2×10^{-4} F/cm^2 with no clear dependence on j_c in the range from 2×10^4 to 2×10^6 A/cm^2 (not shown).

Figure 7(b) shows the normalized excess current density j_e/j_c vs j_c. For the largest values of j_c, we do find excess currents that decay with decreasing j_c and finally disappear at $j_c \approx 2 \times 10^5\,\mathrm{A/cm^2}$. This behavior seems to be independent of the substrate material. The appearance of excess currents has also been reported for cuprate grain-boundary JJs and electron-beam damaged JJs with large current densities [11,16]. Such JJs are often modeled as superconductor–normal-metal–superconductor (S–N–S) JJs. For He-FIB JJs in YBCO films, Cybart *et al.* [28] reported on the transition from S–N–S-type to superconductor-insulator-superconductor-(S–I–S) type JJs upon increasing the irradiation dose. Our results are consistent with this observation; a more detailed analysis, however, requires transport measurements at variable temperature, which we have not performed so far in detail.

To conclude this section, we can state that for obtaining devices that do not exhibit excess currents, one should not exceed $j_c \approx 10^5\,\mathrm{A/cm^2}$. For devices on STO, however, such low j_c values come with values of β_C clearly above 1, i.e., with hysteretic IVCs. The $I_c(B)$ patterns of devices on MgO, on the other hand, show the strongest deviations from a Fraunhofer-like behavior. Hence, at the current state it seems that, among the substrate materials investigated here, He-FIB JJ devices on LSAT are most promising for applications.

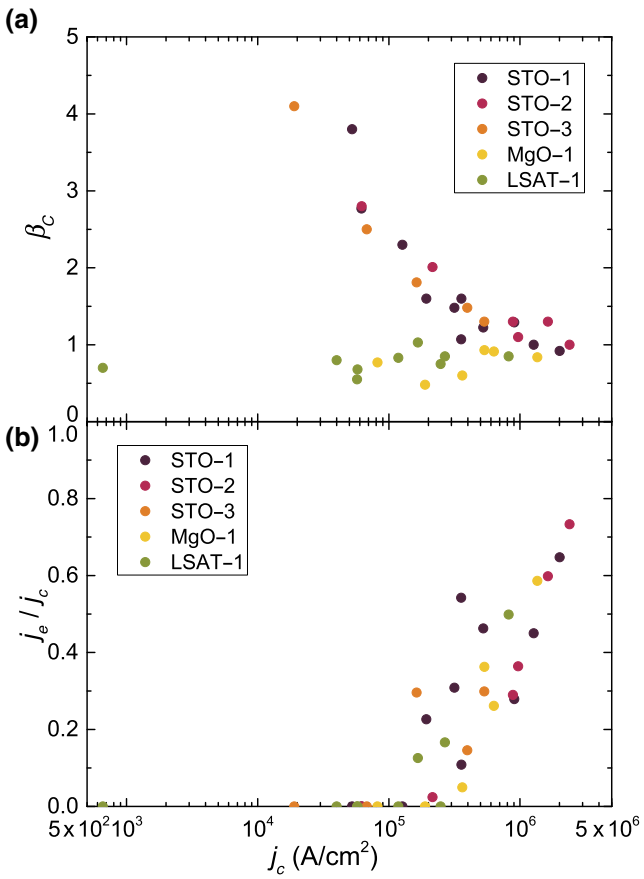

FIG. 7. (a) Stewart-McCumber parameter $\beta_C(j_c)$ and (b) normalized excess current $j_e/j_c(j_c)$ for He-FIB JJs on different substrates.

IV. HE-FIB-INDUCED DC SQUIDS

By irradiation with high He ion doses (typically for $D \gtrsim 1000$ ions/nm), j_c can be fully suppressed, as shown in Fig. 2, and the He-FIB-induced barriers can be made highly resistive (reaching even gigaohm resistances at 4.2 K for $D \gtrsim 5000$ ions/nm). This technique offers the possibility to define the sample geometry—ultimately on the nanometer scale—via direct-write lithography, without removing material by milling [30,31].

The combination of He-FIB irradiation with medium and high doses provides a simple way of fabricating dc SQUIDs from photolithographically prepatterned YBCO thin-film bridges on single-crystal substrates, with tailored JJ properties and SQUID inductance. We use this approach to fabricate simple micro- and nano-SQUIDs on STO, MgO, and LSAT substrates by first scanning over a square-shaped area at the center of the prepatterned YBCO bridge to define the SQUID "hole" (i.e., a highly resistive, magnetically transparent area) and a subsequent linescan across the whole width of the bridge using a medium dose to produce the JJs. A SEM image of such a SQUID is shown in the inset of Fig. 8(a) for a device fabricated on STO-1 with a 1×1-μm^2 hole (irradiated with $D_A = 4000$ ions/nm^2). Again, the locations of the JJs (irradiated with $D = 700$ ions/nm) and the SQUID hole are visible via the He-FIB-induced carbon deposition.

Since the hysteresis in the IVCs severely limits the performance of SQUIDs on STO substrates, the electric-transport and noise data shown in the following are measured on a device fabricated on LSAT-1. On the LSAT substrate, however, SEM imaging is only possible in poor quality due to charging of the substrate. For the device on LSAT, the SQUID hole is defined as a 300×300-nm^2 square, irradiated with $D_A = 4000$ ions/nm^2. The JJs are fabricated by a linescan with $D = 230$ ions/nm and have a width of approximately 2 μm each.

Figure 8(a) shows the IVCs for different applied magnetic flux to yield maximum (black) and minimum (red) positive critical current, exhibiting neither hysteresis nor excess current. From RCSJ simulations, we determine a mean per-junction critical current $I_0 = 43.6$ μA and normal state resistance $R_n = 9.50\,\Omega$ ($V_c = 414$ μV) and $\beta_C = 0.74$. The dependence of the critical current $I_{c,s}$ of the SQUID on the magnetic field is shown in Fig. 8(b) as solid lines, together with the numerically simulated dependence, based on the RCSJ model [50] (symbols). From the simulations, we extract the screening parameter $\beta_L \equiv 2I_cL/\Phi_0 = 0.79$, inductance $L = 19$ pH, and asymmetry parameters [50] for the critical current $\alpha_I = 0.145$ and inductance $\alpha_L = -0.15$. Figure 8(c) shows the voltage-flux dependence of the SQUID for a range of bias currents $I_b \approx \pm 110$ μA in steps of 4 μA. The dark dot near the center on the curve for $I_b = -85$ μA indicates the working point with a transfer function $V_\Phi = 2.1$ mV/Φ_0, which is used for the noise measurement shown in Fig. 9.

To determine the spectral density of flux noise S_Φ vs frequency f of the SQUID, we use Magnicon SEL-1 SQUID electronics [51] in direct readout mode [52]. Figure 9 shows the measured rms spectral density of flux noise $S_\Phi^{1/2}(f)$ of the SQUID (red), together with the background noise of the readout electronics (black). The noise spectrum is dominated by frequency-dependent excess noise, scaling roughly as $S_\Phi \propto 1/f$ ($1/f$ noise), with a small bump (at approximately 10 kHz). This excess noise extends all the way up to the cutoff frequency $f_{el} = 166$ kHz of our readout electronics (limited by the sampling rate of the analog-to-digital converter), where it almost reaches the noise floor of the readout electronics. For YBCO SQUIDs, one typically finds a strong $1/f$ noise contribution due to I_c fluctuations in the JJs [8]. This result is also probably the case for the SQUID presented here. To further clarify this, one should operate the SQUIDs in current-bias reversal mode [53], which eliminates the excess noise contribution from I_c fluctuations. We have already successfully demonstrated this approach for YBCO nano-SQUIDs based on grain-boundary JJs [54]; however, for the simple SQUID layout without a suitable

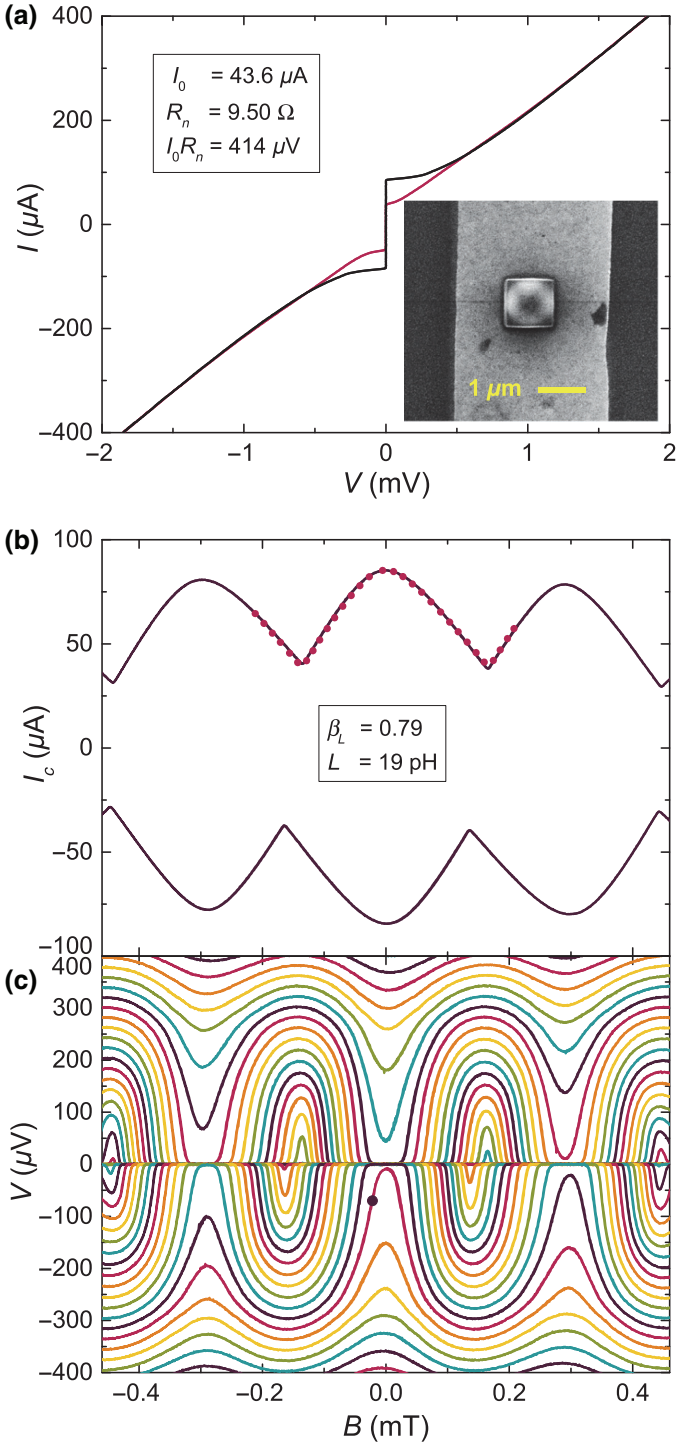

FIG. 8. Electric-transport characteristics of a He-FIB dc SQUID fabricated on LSAT-1-2. (a) IVCs for applied flux yielding maximum (black) and minimum (red) positive critical current. The inset shows a SEM image of a similar SQUID fabricated on STO-1. (b) Critical current vs magnetic field: experimental data (solid lines) and numerical simulation (symbols). (c) Voltage-flux dependence for bias currents I_b within approximately $\pm 110\,\mu$A in steps of $4\,\mu$A. The dark dot near the center indicates the working point for noise measurement.

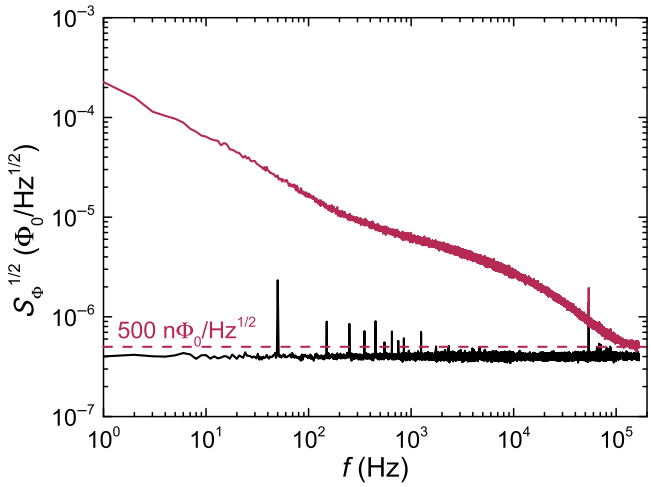

FIG. 9. Noise characteristics of a He-FIB dc SQUID fabricated on LSAT-1-2, with flux noise spectra of the SQUID (red) and electronics background (black). The dashed line indicates the upper limit for thermal white noise $S_{\Phi,w}^{1/2} = 500\,\mathrm{n}\Phi_0/\mathrm{Hz}^{1/2}$ of the SQUID.

on-chip flux coupling structure, as used in this work, it is not possible to use this approach. At least, from the noise data shown in Fig. 9, we can give an upper limit for the thermal white noise $S_{\Phi,w}^{1/2} \lesssim 500\,\mathrm{n}\Phi_0/\mathrm{Hz}^{1/2}$, which is impressively low for a $L \approx 20$ pH SQUID.

V. CONCLUSIONS

We demonstrate the fabrication of YBCO Josephson junctions and dc SQUIDs by using a focused He ion beam, which locally modifies epitaxially grown YBCO thin films and allows us to "write" Josephson barriers and insulating areas with high spatial resolution. The analysis of the electric-transport properties at 4.2 K of our He-FIB-induced structures confirms and extends earlier results obtained by Cybart and co-workers [28–30].

We study in detail the dependence of characteristic JJ properties on the irradiation dose for devices on STO, MgO, and LSAT substrates. Upon increasing the irradiation dose, we find a transition from flux-flow to RCSJ-like behavior with some excess current contribution that vanishes upon further increasing the dose. Moreover, we find an exponential decay of the critical current density j_0 with increasing dose. For currently unclear reasons, this decay is much faster for devices on LSAT as compared to devices on STO and MgO. Another major difference regarding JJ behavior on different substrates is the observation of hysteretic IVCs for devices on STO, while devices on LSAT and MgO show no hysteresis. We attribute the hysteresis in the IVCs to a stray capacitance contribution from the STO substrates. The analysis of the characteristic voltage V_c of the fabricated JJs yields an approximate scaling $V_c \propto \sqrt{j_0}$.

Altogether, He-FIB JJs offer new perspectives for creating Josephson devices, because of the possibility to control the JJ properties by irradiation dose, even on the same substrate, and to place the JJs at virtually arbitrary positions. This flexibility obviously offers an enormous advantage for creating advanced devices, in particular employing multi-JJ configurations. Our detailed analysis of the JJ properties can be helpful for designing optimized devices for applications.

Moreover, irradiation with a high dose drives the material to be highly resistive. In this regime, our STEM analysis shows the creation of amorphous tracks in the YBCO films, which for not-too-high doses still have a lateral extension down to only a few nanometers. This observation indicates that He-FIB irradiation is a promising tool for nanopatterning (without removal of material) of YBCO films with ultrahigh resolution. We use this feature to produce dc SQUIDs by patterning both the JJs and the SQUID loop by He-FIB irradiation. For a device on LSAT, we demonstrate very low flux noise in the thermal white-noise regime. The observed low-frequency excess noise still has to be investigated in detail in further studies. Although we have not yet pushed to the ultimate limit of miniaturization, we envisage that He-FIB irradiation should be ideally suited for the realization of ultralow-noise nano-SQUIDs [55,56] due to the high spatial resolution of helium ion microscopy.

ACKNOWLEDGMENTS

B.M. acknowledges funding by the German Academic Scholarship Foundation. We gratefully acknowledge fruitful discussions with S. Cybart, V.G. Kogan, R.G. Mints, and R. Menditto and technical support by M. Turad and R. Löffler (LISA$^+$), W. Nisch and C. Warres (NMI), and C. Back. This work is supported by the COST action NANOCOHYBRI (Grant No. CA16218).

[1] K. K. Likharev, Superconducting weak links, Rev. Mod. Phys. **51**, 101 (1979).

[2] A. Barone and G. Paternò, *Physics and Applications of the Josephson Effect* (John Wiley & Sons, New York, 1982).

[3] R. Kleiner and W. Buckel, *Superconductivity*, 3rd ed., (Wiley-VCH, Weinheim, 2016).

[4] M. Bhushan and E. M. Macedo, Nb/AlO$_x$/Nb trilayer process for the fabrication of submicron Josephson junctions and low-noise dc SQUIDs, Appl. Phys. Lett. **58**, 1323 (1991).

[5] D. Hagedorn, O. Kieler, R. Dolata, R. Behr, F. Müller, J. Kohlmann, and J. Niemeyer, Modified fabrication of planar sub-μm superconductor-normal metal-superconductor Josephson junctions for use in a Josephson arbitrary waveform synthesizer, Supercond. Sci. Technol. **19**, 294 (2006).

[6] U. Welp, K. Kadowaki, and R. Kleiner, Superconducting emitters of THz radiation, Nat. Photon. **7**, 702 (2013).

[7] T. Ortlepp, Ariando Amd O. Mielke, C. J. M. Verwijs, K. F. K. Foo, H. Rogalla, F. H. Uhlmann, and H. Hilgenkamp, Flip-flopping fractional flux quanta, Science **312**, 1495 (2006).

[8] D. Koelle, R. Kleiner, F. Ludwig, E. Dantsker, John Clarke, High-transition-temperature superconducting quantum interference devices, Rev. Mod. Phys. **71**, 631 (1999).

[9] M. I. Faley, J. Dammers, Y. V. Maslennikov, J. F. Schneiderman, D. Winkler, V. P. Koshelets, N. J. Shah, and R. E. Dunin-Borkowski, High-T_c SQUID biomagnetometers, Supercond. Sci. Technol. **30**, 083001 (2017).

[10] R. Gross, L. Alff, A. Beck, O. M. Froehlich, D. Koelle, and A. Marx, Physics and technology of high temperature superconducting Josephson junctions, IEEE Trans. Appl. Supercond. **7**, 2929 (1997).

[11] H. Hilgenkamp and J. Mannhart, Grain boundaries in high-T_c superconductors, Rev. Mod. Phys. **74**, 485 (2002).

[12] F. Tafuri and J. R. Kirtley, Weak links in high critical temperature superconductors, Rep. Prog. Phys. **68**, 2573 (2005).

[13] F. Tafuri, D. Massarotti, L. Galletti, D. Stornaiuolo, D. Montemurro, L. Longobardi, P. Lucignano, G. Rotoli, G. P. Pepe, A. Tagliacozzo, and F. Lombardi, Recent achievements on the physics of high-T_C superconductor Josephson junctions: Background, perspectives and inspiration, J. Supercond. Nov. Magn. **26**, 21 (2013).

[14] K. Cedergren, J. R. Kirtley, T. Bauch, G. Rotoli, A. Troeman, H. Hilgenkamp, F. Tafuri, and F. Lombardi, Interplay between Static and Dynamic Properties of Semifluxons in $YBa_2Cu_3O_{7-\delta}$ 0-π Josephson Junctions, Phys. Rev. Lett. **104**, 177003 (2010).

[15] S. K. Tolpygo, B. Nadgorny, S. Shokhor, F. Tafuri, Y. Lin, A. Bourdillon, and M. Gurvitch, Electron beam writing in fabricating planar high-T_c Josephson junctions, Phys. C **209**, 211 (1993).

[16] A. J. Pauza, W. E. Booij, K. Herrmann, D. F. Moore, M. G. Blamire, D. A. Rudman, and L. R. Vale, Electron-beam damaged high-temperature superconductor Josephson junctions, J. Appl. Phys. **82**, 5612 (1997).

[17] W. E. Booij, A. J. Pauza, D. F. Moore, E. J. Tarte, and M. G. Blamire, Electrodynamics of closely coupled $YBa_22Cu_3O_{7-\delta}$ junctions, IEEE Trans. Appl. Supercond. **7**, 3025 (1997).

[18] W. E. Booij, C. A. Elwell, E. J. Tarte, P. F. McBrien, F. Kahlmann, D. F. Moore, M. G. Blamire, N. H. Peng, and C. Jeynes, Electrical properties of electron and ion beam irradiated $YBa_22Cu_3O_{7-\delta}$, IEEE Trans. Appl. Supercond. **9**, 2886 (1999).

[19] K. Chen, S. A. Cybart, and R. C. Dynes, Planar thin film $YBa_2Cu_3O_{7-\delta}$ Josephson junction pairs and arrays via nanolithography and ion damage, Appl. Phys. Lett. **85**, 2863 (2004).

[20] K. Chen, S. A. Cybart, and R. C. Dynes, Study of closely spaced $YBa_2Cu_3O_{7-\delta}$ Josephson junction pairs, IEEE Trans. Appl. Supercond. **15**, 149 (2005).

[21] S. S. Tinchev, Investigation of RF SQUIDs made from epitaxial YBCO films, Supercond. Sci. Technol. **3**, 500 (1990).

[22] N. Bergeal, X. Grison, J. Lesueur, G. Faini, M. Aprili, and J. P. Contour, High-quality planar high-T_c Josephson junctions, Appl. Phys. Lett. **87**, 102502 (2005).

[23] W. C. Stewart, Current-voltage characteristics of Josephson junctions, Appl. Phys. Lett. **12**, 277 (1968).

[24] D. E. McCumber, Effect of ac impedance of dc voltage-current characteristics of Josephson junctions, J. Appl. Phys. **39**, 3113 (1968).

[25] S. A. Cybart, P. X. T. Yen, E. Y. Cho, J. U. Huh, V. N. Glyantsev, C. S. Yung, B. Moeckly, J. W. Beeman, and R. C. Dynes, Comparison of Y–Ba–Cu–O films irradiated with helium and neon ions for the fabrication of Josephson devices, IEEE Trans. Appl. Supercond. **24**, 1100105 (2014).

[26] W. Lang, and J. D. Pedarnig, in *Nanoscience and Enigneering in Superconductivity*, edited by V. Moshchalkov, R. Wördenweber, and W. Lang (Springer Verlag, Berlin Heidelberg, 2010) Chap. 3, p. 81.

[27] G. Hlawacek and A. Gölzhäuser, eds., *Helium Ion Microscopy* (Springer International Publishing, Cham, Switzerland, 2016).

[28] S. A. Cybart, E. Y. Cho, J. T. Wong, B. H. Wehlin, M. K. Ma, C. Huynh, and R. C. Dynes, Nano Josephson superconducting tunnel junctions in $YBa_2Cu_3O_{7-\delta}$ directly patterned with a focused helium ion beam, Nat. Nano **10**, 598 (2015).

[29] E. Y. Cho, M. K. Ma, C. Huynh, K. Pratt, D. N. Paulson, V. N. Glyantsev, R. C. Dynes, and S. A. Cybart, $YBa_2Cu_3O_{7-\delta}$ superconducting quantum interference devices with metallic to insulating barriers written with a focused helium ion beam, Appl. Phys. Lett. **106**, 252601 (2015).

[30] E. Y. Cho, Y. W. Zhou, J. Y. Cho, and S. A. Cybart, Superconducting nano Josephson junctions patterned with a focused helium ion beam, Appl. Phys. Lett. **113**, 022604 (2018).

[31] E. Y. Cho, H. Li, J. C. LeFebvre, Y. W. Zhou, R. C. Dynes, and S. A. Cybart, Direct-coupled micro-magnetometer with Y-Ba-Cu-O nano-slit SQUID fabricated with a focused helium ion beam, Appl. Phys. Lett. **113**, 162602 (2018).

[32] S. Cybart, R. Bali, G. Hlawacek, F. Röder, and J. Fassbender, in *Helium Ion Microscopy*, edited by G. Hlawacek and A. Gölzhäuser (Springer International Publishing, Cham, Switzerland, 2016) Chap. 17, p. 415.

[33] A. Gozar, N. E. Litombe, Jennifer E. Hoffman, and I. Bozovic, Optical nanoscopy of high T_c cuprate nanoconstriction devices patterned by helium ion beams, Nano Lett. **17**, 1582 (2017).

[34] L. Kasaei, T. Melbourne, V. Manichev, L. C. Feldman, T. Gustafsson, Ke Chen, X. X. Xi, and B. A. Davidson, MgB_2 Josephson junctions produced by focused helium ion beam irradiation, AIP Adv. **8**, 075020 (2018).

[35] R. Werner, C. Raisch, A. Ruosi, B. A. Davidson, P. Nagel, M. Merz, S. Schuppler, M. Glaser, J. Fujii, T. Chassé, R. Kleiner, and D. Koelle, $YBa_2Cu_3O_7/La_{0.7}Ca_{0.3}MnO_3$ bilayers: Interface coupling and electric transport properties, Phys. Rev. B **82**, 224509 (2010).

[36] T. Schwarz, J. Nagel, R. Wölbing, M. Kemmler, R. Kleiner, and D. Koelle, Low-noise nano superconducting quantum interference device operating in tesla magnetic fields, ACS Nano **7**, 844 (2013).

[37] R. Gross, P. Chaudhari, D. Dimos, A. Gupta, and G. Koren, Thermally Acitvated Phase Slippage in High-T_c Grain-boundary Josephson Junctions, Phys. Rev. Lett. **64**, 228 (1990).

[38] R. Wölbing, T. Schwarz, B. Müller, J. Nagel, M. Kemmler, R. Kleiner, and D. Koelle, Optimizing the spin sensitivity of grain boundary junction nanoSQUIDs – Towards detection of small spin systems with single-spin resolution, Supercond. Sci. Technol. **27**, 125007 (2014).

[39] L. Thiel, D. Rohner, M. Ganzhorn, P. Appel, E. Neu, B. Müller, R. Kleiner, D. Koelle, and P. Maletinsky, Quantitative nanoscale vortex imaging using a cryogenic quantum magnetometer, Nat. Nanotechnol. **11**, 677 (2016).

[40] M. J. Martínez-Pérez, B. Müller, D. Schwebius, D. Korinski, R. Kleiner, J. Sesé, and D. Koelle, NanoSQUID magnetometry of individual cobalt nanoparticles grown by focused electron beam induced deposition, Supercond. Sci. Technol. **30**, 024003 (2017).

[41] D. Rohner, L. Thiel, B. Müller, M. Kasperczyk, R. Kleiner, D. Koelle, and P. Maletinsky, Real-space probing of the local magnetic response of thin-film superconductors using single spin magnetometry, Sensors **18**, 3790 (2018).

[42] M. Moshe, V. G. Kogan, and R. G. Mints, Edge-type Josephson junctions in narrow thin-film strips, Phys. Rev. B **78**, 020510 (2008).

[43] A. A. Abdumalikov Jr., G. L. Alfimov, and A. S. Malishevskii, Nonlocal electrodynamics of Josephson vortices in superconducting circuits, Supercond. Sci. Technol. **22**, 023001 (2009).

[44] John R. Clem, Josephson junctions in thin and narrow rectangular superconducting strips, Phys. Rev. B **81**, 144515 (2010).

[45] A. A. Boris, A. Rydh, T. Golod, H. Motzkau, A. M. Klushin, and V. M. Krasnov, Evidence for Nonlocal Electrodynamics in Planar Josephson Junctions, Phys. Rev. Lett. **111**, 117002 (2013).

[46] V. G. Kogan and R. G. Mints, Manipulating Josephson junctions in thin-films by nearby vortices, Phys. C **502**, 58 (2014).

[47] R. Gross and B. Mayer, Transport processes and noise in $YBa_2Cu_3O_{7-\delta}$ grain boundary junctions, Phys. C **180**, 235 (1991).

[48] S. Graser, P. J. Hirschfeld, T. Kopp, R. Gutser, B. M. Andersen, and J. Mannhart, How grain boundaries limit supercurrents in high-temperature superconductors, Nature Phys. **6**, 609 (2010).

[49] A. Beck, A. Stenzel, O. M. Froehlich, R. Gerber, R. Gerdemann, L. Alff, B. Mayer, R. Gross, A. Marx, J. C. Villegier, and H. Moriceau, Fabrication and superconducting transport properties of bicrystal grain boundary Josephson junctions on different substrates, IEEE Trans. Appl. Supercond. **5**, 2192 (1995).

[50] B. Chesca, R. Kleiner, and D. Koelle, in *The SQUD Handbook*, Vol. 1: Fundamentals and Technology of SQUIDs and SQUID systems, edited by John Clarke and Alex I. Braginski (Wiley-VCH, Weinheim, 2004) Chap. 2, p. 29.

[51] SQUID electronics SEL-1 from Magnicon GmbH, Lemsahler Landstr. 171, D-22397 Hamburg, Germany; http://www.magnicon.com.

[52] D. Drung, High-T_c and low-T_c dc SQUID electronics, Supercond. Sci. Technol. **16**, 1320 (2003).

[53] D. Drung, and M. Mück, in *The SQUD Handbook, Vol. 1: Fundamentals and Technology of SQUIDs and SQUID systems*, edited by John Clarke and Alex I. Braginski, (Wiley-VCH Weinheim, 2004) Chap. 4, p. 127.

[54] T. Schwarz, R. Wölbing, C. F. Reiche, B. Müller, M. J. Martínez-Pérez, T. Mühl, B. Büchner, R. Kleiner, and D. Koelle, Low-noise $YBa_2Cu_3O_7$ Nano-SQUIDs for Performing Magnetization-reversal Measurements on Magnetic Nanoparticles, Phys. Rev. Appl. **3**, 044011 (2015).

[55] C. Granata and A. Vettoliere, Nano superconducting quantum interference device: A powerful tool for nanoscale investigations, Phys. Rep. **614**, 1 (2016).

[56] M. J. Martínez-Pérez and D. Koelle, NanoSQUDs: Basics & recent advances, Phys. Sci. Rev. **2**, 20175001 (2017).